Theor Chem Acc (2011) 130:765–774
DOI 10.1007/s00214-011-0968-y

REGULAR ARTICLE

Orbital views of the electron transport through heterocyclic aromatic hydrocarbons

Xinqian Li · Aleksandar Staykov · Kazunari Yoshizawa

Received: 1 February 2011 / Accepted: 19 May 2011 / Published online: 16 June 2011

Abstract Electron-transport properties of heterocyclic aromatic hydrocarbons are investigated with theoretical methods. The present study is based on a previously derived concept for orbital control of electron transport through aromatic hydrocarbons. The orbital control concept provided crucial basic understanding for the best conductance channels in the aromatic hydrocarbons and was successfully applied in the design of molecular devices. That concept was proven to hold true for small aromatic molecules, large polycyclic aromatic hydrocarbons with different edge structures, and in weak and strong coupling with the electrodes junctions. The polycyclic aromatic hydrocarbons and nanographenes used in the molecular electronics are often immobilized with different types of defects, which require the application of the orbital control concept on heterocyclic aromatic hydrocarbons. In this work, the effect of the heteroatoms in aromatic hydrocarbons on their electron-transport properties and the applicability of the orbital control concept on heterocyclic aromatic hydrocarbons are studied. Effective routes for electron transport are predicted in weak coupling junctions by analyzing the phase and amplitude of the frontier orbitals. The qualitative predictions are made with the nonequilibrium Green's function method combined with the Hückel approximation. Quantitative, first principle calculations are performed with the nonequilibrium Green's function method combined with density functional theory. The obtained results are in good agreement with the expectations on the basis of the orbital control concept, which proves its applicability in heterocyclic aromatic hydrocarbons.

Keywords Nonequilibrium Green's function · Orbital symmetry rule · Electron-transport properties · Heterocyclic aromatic hydrocarbons

1 Introduction

With recent advances in miniaturization, electronic elements are rapidly approaching molecular scales. Molecular electronics deals with properties of single molecules or molecular assemblies capable of reproducing and replacing the functions of classical electronic devices. New carbon materials such as graphenes [1] are of recent, special interest among the structurally diverse range of single molecules for molecular electronics. Müllen and coworkers [2] have introduced a bottom-up synthetic approach for controlled building of nanographenes from benzene. This synthetic concept allows for the design and fabrication of large polycyclic aromatic hydrocarbons (PAHs) with known edge structure, symmetry, size, and shape. Consequently, it is now possible to fabricate PAHs with defect states where the exact location of the defect and its type are known. While PAHs possess interesting electronic properties, the most exciting physical phenomena, which can lead to the industrial fabrication of electronic devices, are due to defect states in the nanographene structure. These defect states are often responsible for electrical and magnetic properties and sensor- and transistor-like properties. Experimental and theoretical studies are intended to understand the underlying electron-transport properties and

Dedicated to Professor Akira Imamura on the occasion of his 77th birthday and published as part of the Imamura Festschrift Issue.

X. Li · A. Staykov · K. Yoshizawa (✉)
Institute for Materials Chemistry and Engineering
and International Research Center for Molecular Systems,
Kyushu University, Fukuoka 819-0395, Japan
e-mail: kazunari@ms.ifoc.kyushu-u.ac.jp

mechanisms through molecules and nanomaterials and help us to identify appropriate nanoscale structures for effective elements in the electronic devices. A variety of experimental techniques, such as scanning tunneling microscopy (STM) [3–6], atomic force microscopy (AFM) [7, 8], and mechanically controllable break junctions (MCBJ) [9–11], have been developed for over a decade. These techniques allowed us to measure the single molecule electron-transport properties such as conductance, current–voltage characteristics, and resistance. These experimental techniques were employed in the actual fabrication of single molecule devices with desired properties [12, 13]. Corresponding to the experimental development, a number of different modern theories of molecular electronics have been used to calculate the electron-transport properties of molecular junctions, such as tunneling transport model [14–16], hopping electron transport model [17, 18], and free-electron network model [19]. These theoretical methods provided an inside view for better understanding the electron transport processes through molecular junctions. Within the coherent electron transport regime, the nonequilibrium Green's function method (NEGF) [20] and Landauer's theory [21] are commonly used to describe the important factors that control the conductance, i.e., the conductance channels, the electron transmission probability, and the change of the transmission probability with the applied bias [16, 22, 23]. In a molecular device, the electron-transport properties are determined not only by the molecule part, but also by the interactions between molecules and electrodes, such as contact bond length and angle [24–26] and anchoring group [27–29]. Moreover, the orbital density distributions on the molecular end groups and the degree of conjugation have been found as significant factor for achieving high conductance values. Ratner and co-workers investigated the coherent conductance of conjugated aromatic molecules with different conjugation levels and different lengths and gave explanations in terms of frontier orbital views [30]. The local transmission through a molecule shows a relationship between molecular structure and electronic couplings, in which the through-space contributions and the ring currents are important interference effects in the electron transport [31]. A perturbation approach was developed for calculating the electronic matrix elements for electron-transfer reactions between a donor and an acceptor linked by large or small bridges, which treated the diagonalization of the entire donor-bridge-acceptor matrix system rather than only the bridge part, and obtained reasonable results [32]. Recently, the quatum interference in electron transport has been demonstrated to be closely related to the topology of molecule's π system, and a simple graphical scheme to predict the existence of quatum interference effects has been proposed by Markussen and co-workers [33], which is based on a simple tight-binding model of the π-electron system.

We have investigated important variations of conductance for different connection sites in aromatic hydrocarbons in terms of orbital phase and amplitude [34–40]. Although the electron transport through a single molecule can be described mainly as a physical phenomenon, one of the most important factors that control it has a discrete chemical origin, the phase, amplitude, and spatial distribution of the frontier orbitals of molecules. These orbital features are essential factors that determine the electron transport through a single molecule. In a previous study, an orbital symmetry rule has been investigated in detail for predicting electron-transport properties in metal–molecule–metal junctions [34, 35, 37].

We would like to briefly review the basic method for calculating molecular conductance. According to Landauer's formula, the conductance of the molecular junction at the zero temperature and zero bias voltage is related to the transmission probability T at the Fermi level E_F of the electrodes, as shown in Eq. 1 [21, 41]:

$$g = \frac{2e^2}{h} T(E_F), \tag{1}$$

where $2e^2/h$ is the quantum conductance. The transmission probability is given by

$$T(E) = \mathrm{Trace}[\Gamma_L(E) G^A(E) \Gamma_R(E) G^R(E)]. \tag{2}$$

The matrix elements of G^A and G^R are advanced and retarded Green's functions, respectively. The broadening function Γ_L and Γ_R describes the coupling of the molecule to the left and right leads, respectively, and the elements of the matrixes can be obtained from the corresponding self-energies of left and right electrodes Σ_L and Σ_R [41]:

$$\Gamma_L = i[\Sigma_L(E) - \Sigma_L^{\dagger}(E)] \tag{3}$$

$$\Gamma_R = i[\Sigma_R(E) - \Sigma_R^{\dagger}(E)]. \tag{4}$$

For the simple molecular device shown in Scheme 1, the Green's function is given by the following matrix:

$$G = \begin{pmatrix} G_L & G_{L,C} & 0 \\ G_{C,L} & G_C & G_{C,R} \\ 0 & G_{R,C} & G_R \end{pmatrix}, \tag{5}$$

where G_L is the Green's function of the left electrode, G_C of the central region, and G_R of the right electrode. $G_{L,C}$, $G_{C,L}$, and $G_{R,C}$, $G_{C,R}$ represent the interactions between the central region with the left and the right electrodes, respectively. The two zero values in the matrix are the

neglect of the interactions between the two electrodes $G_{L,R}$ and $G_{R,L}$, since the two electrodes have no contact with each other as shown in Scheme 1. From the definition of the Green's function [41]:

$$G(E) = [EI - H]^{-1}, \tag{6}$$

where I is the unit matrix and H is the Hamiltonian of the system, Eq. 5 can be written in the following form:

$$G(E) = \begin{pmatrix} EI_L - H_L & -H_{L,C} & 0 \\ -H_{C,L} & EI_C - H_C & -H_{C,R} \\ 0 & -H_{R,C} & EI_R - H_R \end{pmatrix}^{-1}. \tag{7}$$

In Eq. 7, H_L is the Hamiltonian of the left electrode, H_c of the central region, and H_R of the right electrode. $H_{L,C}$, $H_{C,L}$, and $H_{R,C}$, $H_{C,R}$ represent the Hamiltonian matrixes of the contacts of the central region with the left and the right electrodes, respectively. A major computational difficulty in Eq. 7 is the different dimensions of H_L, H_C, and H_R. While the central region has a finite number of atoms, i.e., a finite Hamiltonian matrix, the size of each electrode is semi-infinite, i.e., H_L and H_R are infinite. A series of linear algebraic transformations [41] reduces the dimensions of Eq. 7 to the finite dimension of the central region. Let us then write the Green's function of the central region in the following form:

$$G_C^R(E) = [EI_C - H_C - \Sigma_L - \Sigma_R]^{-1}. \tag{8}$$

In Eq. 8, the self-energies of the left and right electrodes Σ_L and Σ_R depend on the Green's functions of the electrodes and the anchoring between the electrodes and the central region. G^A and G^R are easily derived from Eq. 6 and are given in Eqs. 9 and 10 [41]:

$$G^R(E) = [(E + i\eta)I_C - H_C - \Sigma_L - \Sigma_R]^{-1} \tag{9}$$

$$G^A(E) = [G^R(E)]^\dagger, \tag{10}$$

where η is an infinitesimal number determined by a relationship between the local density of states (LDOS) and the imaginary part of zeroth Green's function [35, 36, 42].

The orbital symmetry rule was proposed on the basis of a molecular junction structure, which is composed of a molecule and two linear gold chains as shown in Fig. 1.

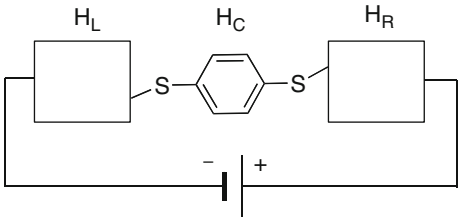

Scheme. 1 Model of a simple molecular device: the central region is in contact with the left and right electrodes

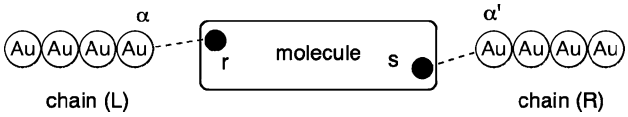

Fig. 1 Schematic representation of a chain–molecule–chain junction, in which the molecule is weakly connected to the gold electrodes

The molecule is connected to two gold atoms α and α' from both gold chains with atoms r and s, respectively.

The relationship between Green's function $G^{A/R}$ and the zeroth Green's functions $G^{(0)A/R}$ was obtained as $G^{A/R} = G^{(0)A/R}/D^{R/A}$ [36, 43, 44]. For a weak coupling system, which has no chemical bonding between the electrodes and molecule, the denominator $D^{R/A}$ could be approximated by one. Therefore, the Green's function $G^{A/R}$ can be viewed as a linear function of the zeroth Green's functions $G^{(0)A/R}$ obtained separately for the two gold electrodes and the molecule [38]. The zeroth Green's function can be written in terms of molecular orbital (MO) coefficients as follow:

$$G_{rs}^{(0)R/A}(E) = \sum_k \frac{C_{rk}C_{sk}^*}{E - \varepsilon_k \pm i\eta}. \tag{11}$$

In Eq. 11, C_{rk} is the kth MO coefficient at atom site r, ε_k is the kth MO energy. The relationship between MOs and Green's function makes it possible to predict the conductance from the MOs. When the Fermi energy is assumed to be located at the midgap of the highest occupied molecular orbital (HOMO) and the lowest unoccupied molecular orbital (LUMO), the contribution of k plays a significant role in zeroth Green's function for the molecule at the Fermi energy because of the smallest denominators, as shown in Eq. 12 [34, 37]:

$$\frac{C_{r\mathrm{HOMO}}C_{s\mathrm{HOMO}}^*}{E_F - \varepsilon_{\mathrm{HOMO}} \pm i\eta} + \frac{C_{r\mathrm{LUMO}}C_{s\mathrm{LUMO}}^*}{E_F - \varepsilon_{\mathrm{LUMO}} \pm i\eta}. \tag{12}$$

To obtain a large transmission probability, the value of Eq. 12 should be large. Since the signs of the denominators $E_F - \varepsilon_{\mathrm{HOMO}}$ and $E_F - \varepsilon_{\mathrm{LUMO}}$ are different, when the sign of $C_{r\mathrm{HOMO}}C_{s\mathrm{HOMO}}^*$ is different from that of $C_{r\mathrm{LUMO}}C_{s\mathrm{LUMO}}^*$, the contributions from the HOMO and LUMO are enhanced and good transmission probability can be obtained. On the other hand, when the signs of the two products are same, the contributions of the HOMO and LUMO are canceled. Large contributions from the HOMO and LUMO are related to the large values of MO expansion coefficients. The orbital symmetry rule for electron-transport properties is summarized as follows [34, 37]: for effective electron transport in a molecular junction, (1) the sign of $C_{r\mathrm{HOMO}}C_{s\mathrm{HOMO}}^*$ should be different from the sign of $C_{r\mathrm{LUMO}}C_{s\mathrm{LUMO}}^*$ and (2) atoms, for which the amplitudes of the HOMO and LUMO are large, should be connected with the electrodes. The necessary conditions to derive the orbital symmetry rule are that (1) the coupling

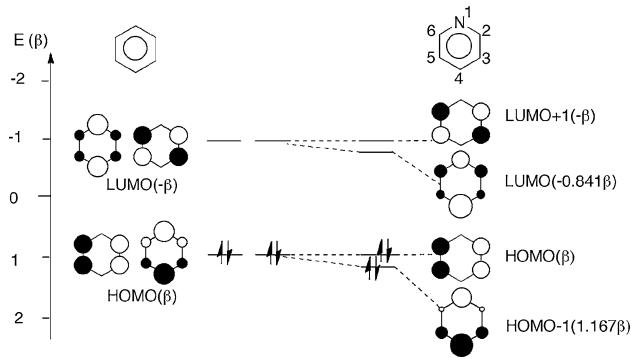

Fig. 2 Molecular orbitals diagram near the Fermi level of benzene and pyridine

between the molecule and electrodes is weak, (2) there is electron–hole symmetry in orbital energies and orbital expansion coefficients, and (3) the Fermi energy is located at the midgap of the HOMO and LUMO. We have investigated the importance of MOs for the electron transport through different systems, such as graphene sheets [34–36] and conducting polymers [45], and we have succeeded to apply the orbital symmetry rule to small-size aromatic hydrocarbons [37], PAHs with different molecular sizes and edge type structures [40], photoswitching systems [38, 39], and strong coupled molecules with the electrodes [46]. According to the orbital analysis of the phase and amplitude of the HOMO and LUMO, we could easily predict possible connections and choose favorable atoms of the molecule to connect with electrodes for effective electron transport. In this paper, we consider heterocyclic aromatic hydrocarbons as models of PAHs with impurity defects. The orbital control rule is applied to the following nitrogen-containing heterocyclic molecules: pyridine, quinoline, isoquinoline, benzo[g]quinoline, and benzo[g]isoquinoline. Our purpose is to investigate the electron transport phenomena of these molecules when connected at different sites to the electrodes to test the applicability of the orbital symmetry rule, and to estimate the effect of the heteroatomic perturbation on the orbitals. The electron-transport properties are investigated with the nonequilibrium Green's function method combined with the Hückel method (NEGF–HMO). We also perform more quantitative calculations using realistic molecular junctions of various dithiolate derivatives of these molecules with the nonequilibrium Green's function method combined with density functional theory (NEGF–DFT) to compare and verify the results of the qualitative predictions based on the orbital concept. In the dithiolate derivatives' molecular junctions, the coupling between molecules and electrodes is strong since the molecules are connected to the electrodes via covalent Au–S bonds [47].

2 Calculation details

Electron-transport properties of the molecules, weakly interacting with the linear gold chain at different atom sites, were investigated by NEGF-HMO method using the formulism given in Eqs. 1–10. In the simple Hückel approximation, the resonance integrals $\beta_{\text{C-Au}}$ and $\beta_{\text{Au–Au}}$ are given the same values used in the previous studies: $\beta_{\text{C–Au}} = 0.2\ \beta_{\text{C–C}}$ and $\beta_{\text{Au–Au}} = 0.6\ \beta_{\text{C–C}}$, respectively [37]. The Coulomb integral α_{N} and resonance integral $\beta_{\text{C–N}}$ for nitrogen atom are $\alpha_{\text{N}} = 0.5\ \beta_{\text{C–C}}$ and $\beta_{\text{C–N}} = \beta_{\text{C–C}}$, respectively [48]. The transmission spectra were obtained for pyridine, quinoline, benzo[*g*]quinoline, isoquinoline, and benzo[g]isoquinoline.

The qualitative predictions were compared with calculations based on the NEGF–DFT method carried out in the ATK 2008.10 program [49] for more realistic molecular junctions, in which two semi-infinite Au (111) electrodes are connected through covalent Au–S bonds [47] of dithiolate derivatives of the π-conjugated molecules. The adsorption site of the dithiolate derivatives used in this study is the fcc threefold hollow site. The semi-infinite left and right electrodes were modeled by two Au(111)-(3 × 3) surfaces. A single-ζ basis set with polarization (SZP) was used for the gold atoms, and double-ζ basis set with polarization (DZP) was used for all other atoms of the molecular part [20]. We performed the electron transport calculations to obtain transmission spectra and *I–V* curves under applied biases in the range from 0.0 to 1.0 V. Prior to the electron transport calculations, geometry optimizations were performed with the Gaussian 03 program [50] at the B3LYP [51–53] level of theory. Models for geometry optimization include one Au atom from the electrodes connected to each S atom. The 6-31G(d) basis set [54] was used for the C, H, and S atoms, and the LANL2DZ basis set [55] was used for the Au atoms. The main features in the

Table 1 Values of the molecular orbitals coefficients of pyridine for different connections

Connection sites ($r - s$)	2–5	2–6	2–4	3–5
$C_{r\text{HOMO}-1}C^*_{s\text{HOMO}-1} + C_{r\text{HOMO}}C^*_{s\text{HOMO}}$	−0.3165	−0.2137	−0.1139	−0.1283
$C_{r\text{LUMO}}C^*_{s\text{LUMO}}+C_{r\text{LUMO}+1}C^*_{s\text{LUMO}+1}$	0.3371	−0.116	−0.2073	−0.1933

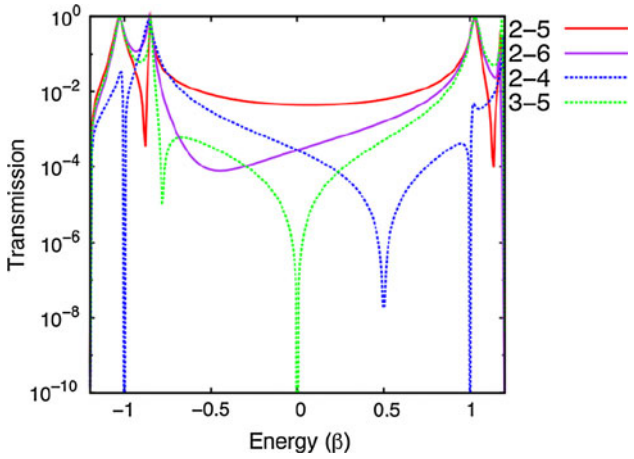

Fig. 3 Transmission spectra for the predicted routes of pyridine calculated with the NEGF–HMO method. Two to five is the symmetry-allowed route for electron transport indicated with *red solid line*, and 2–6, 2–5, and 3–5 are symmetry-forbidden routes indicated with *dashed lines*

transmission spectrum were not affected significantly when using the model optimized with three gold atoms from the Au (111) surface on each side of the molecules [46].

3 Results and discussion

According to the orbital symmetry rule, it is possible to predict the symmetry-allowed and symmetry-forbidden connections for the transmission probabilities in heterocyclic aromatic hydrocarbons. Figure 2 shows the molecular orbitals diagram of benzene and pyridine. The HOMOs and LUMOs of benzene are used to construct the HOMO and LUMO of pyridine. The degeneracy of the frontier orbitals in benzene is broken in pyridine due to the perturbation cause by the N atom. As a result the double degenerate HOMOs and LUMOs are split into relatively close-lying HOMO–1 and HOMO and relatively close-lying LUMO and LUMO+1, respectively. In the HOMO–1 of pyridine, the electron density is increased on the nitrogen and the two *meta*-carbon (C3 and C5) atoms, and the amplitudes at the *para* (C4) and two *ortho* (C2 and C6) positions have increased in LUMO, correspondingly. When using the orbital symmetry rule to predict the electron-transport properties of pyridine, we should look back to Eq. 11. Because the HOMO–1 and LUMO+1 are located close in energy to the HOMO and LUMO, the denominators in Eq. 11 do not change much. The contributions of the HOMO–1 and LUMO+1 in the numerators are nearly the same as those for the frontier orbitals and should not be neglected. Thus, we need to consider not only the HOMO and LUMO, but also the HOMO–1 and LUMO+1 of pyridine in the orbital symmetry rule. We have to look at the sign of $C_{r\mathrm{HOMO}-1}C^*_{s\mathrm{HOMO}-1} + C_{r\mathrm{HOMO}}C^*_{s\mathrm{HOMO}}$ and the sign of $C_{r\mathrm{LUMO}}C^*_{s\mathrm{LUMO}} + C_{r\mathrm{LUMO}+1}C^*_{s\mathrm{LUMO}+1}$, in which r and s indicate the atoms of the molecule connected to (in contact with) the two gold atoms. The results for these orbital coefficients with different connection sites are shown in Table 1. For connection 2–5, the signs of $C_{r\mathrm{HOMO}-1}C^*_{s\mathrm{HOMO}-1} + C_{r\mathrm{HOMO}}C^*_{s\mathrm{HOMO}}$ and $C_{r\mathrm{LUMO}}C^*_{s\mathrm{LUMO}} + C_{r\mathrm{LUMO}+1}C^*_{s\mathrm{LUMO}+1}$ are different, and the absolute values are large. Enhanced contribution from these MOs occurs in Eq. 11. Therefore, it is expected that connection 2–5 is a symmetry-allowed connection characterized with high conductance. For connections 2–6, 2–4, and 3–5, the signs of those two sums of products are the same. Therefore, according to the orbital symmetry rule, those connections are symmetry forbidden and they lead to low conductance.

The transmission spectra for connections 2–4, 2–5, 2–6, and 3–5 of pyridine are calculated with the NEGF–HMO method and are shown in Fig. 3. The solid line shows the symmetry-allowed connection, whereas the dashed lines show the symmetry-forbidden connections. The symmetry-allowed connection 2–5 shows the highest transmission probabilities at the Fermi energy, which is consistent with the qualitative predictions.

Symmetry-forbidden connection 3–5 shows no transmission probabilities at the Fermi energy. However, in the transmission spectra of connections 2–4 and 2–6, the transmission probabilities at the Fermi energy are different from zero, and deep peaks at electron energies 0.5β and -0.5β are observed, respectively. The reason for those deep peaks can be traced back to the orbital coefficients' values for connections 2–4 and 2–6, which are reported in Table 1. The corresponding values of these two connections show the same signs but very different values. Since the Fermi energy is set at the midgap of the HOMO and LUMO, the contributions of MOs are not completely canceled at the Fermi energy in connections 2–4 and 2–6. Moreover, we define the portions/contributions of frontier orbitals to $G^{(0)}_{rs}$ according to Eq. 11 separately as follows:

Table 2 Values of the portion zeroth Green's function of pyridine for different connections

Connection sites ($r - s$)	2–5	2–6	2–4	3–5
$G^{(0)}_{rs(\mathrm{HOMO,\ HOMO}-1)}$	−0.332	−0.238	−0.105	−0.160
$G^{(0)}_{rs(\mathrm{LUMO,\ LUMO}+1)}$	−0.326	0.086	0.225	0.170

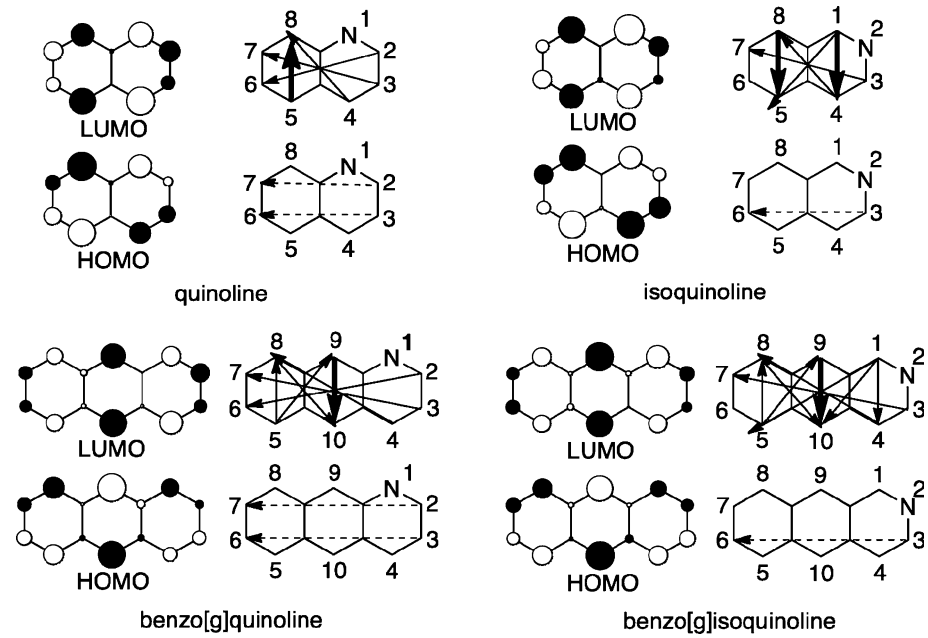

Fig. 4 Frontier orbitals of quinoline, isoquinoline, benzo[g]quinoline, and benzo[g]isoquinoline calculated with the Hückel method. Symmetry-allowed and symmetry-forbidden routes for electron transport are indicated with *solid* and *dashed arrows*, respectively

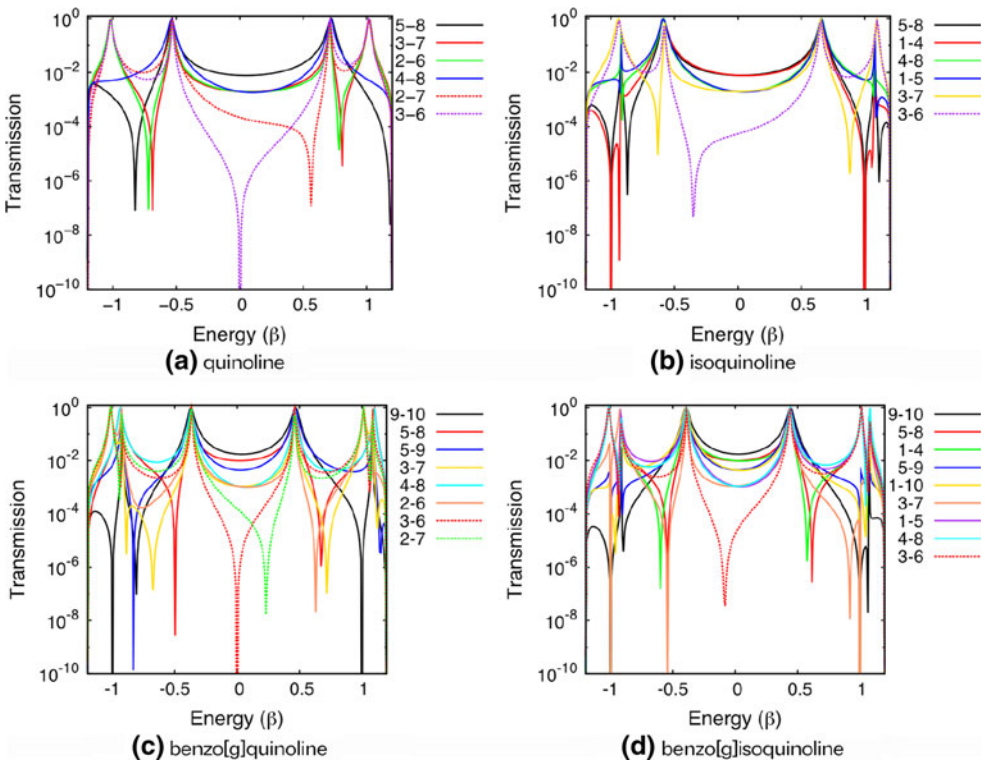

Fig. 5 Transmission spectra for the predicted routes calculated with the NEGF–HMO method: **a** quinoline, **b** isoquinoline, **c** benzo[g]quinoline, and **d** benzo[g]isoquinoline

$$G^{(0)}_{rs(\mathrm{HOMO,HOMO-1})} \equiv \frac{C_{r\mathrm{HOMO}}C^{*}_{s\mathrm{HOMO}}}{E_{\mathrm{F}}-\varepsilon_{\mathrm{HOMO}}} + \frac{C_{r\mathrm{HOMO-1}}C^{*}_{s\mathrm{HOMO-1}}}{E_{\mathrm{F}}-\varepsilon_{\mathrm{HOMO-1}}} \quad (13)$$

$$G^{(0)}_{rs(\mathrm{LUMO,LUMO+1})} \equiv \frac{C_{r\mathrm{LUMO}}C^{*}_{s\mathrm{LUMO}}}{E_{\mathrm{F}}-\varepsilon_{\mathrm{LUMO}}} + \frac{C_{r\mathrm{LUMO+1}}C^{*}_{s\mathrm{LUMO+1}}}{E_{\mathrm{F}}-\varepsilon_{\mathrm{LUMO+1}}}. \quad (14)$$

On the basis of orbital symmetry rule, E_{F} is assumed to be located in the midgap of HOMO and LUMO of pyridine with an energy of 0.08β. The contributions from the HOMO, HOMO-1 and LUMO, LUMO+1 to $G^{(0)}_{rs}$ are shown in Table 2. The enhanced contribution from these MOs is observed in connection 2–5, which shows high conductance. The values of $G^{(0)}_{rs(\mathrm{HOMO,\ HOMO-1})}$ and $G^{(0)}_{rs(\mathrm{LUMO,\ LUMO+1})}$ for connections 2–6 and 2–4 are almost

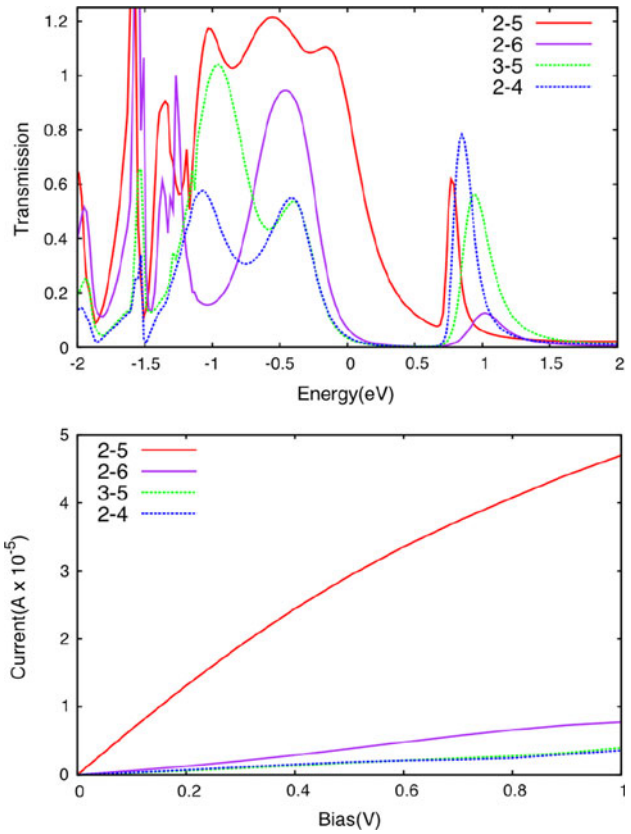

Fig. 6 Calculated transmission spectra at the zero bias and *I–V* curves for pyridine dithiolate junctions at the Perdew–Zunger LDA level of theory

half canceled. Thus, the deep peaks in the transmission spectra are shifted from the Fermi energy. The cancelation occurred completely in symmetry-forbidden connection 3–5 with the values of −0.160 and 0.170, which results in the zero transmission probabilities at Fermi energy.

The frontier orbitals of quinoline, isoquinoline, benzo[g]quinoline, and benzo[g]isoquinoline obtained from Hückel calculations, as well as the predicted routes for electron transport are shown in Fig. 4. For these molecules, the HOMO–1 and LUMO+1 are not close in energy to the HOMO and LUMO, which is the major difference from pyridine. That is why the transmission probabilities can be predicted only by looking at the frontier orbitals. The solid arrows in Fig. 4 show the predicted symmetry-allowed connections with high transmission probabilities; the dashed arrows show the predicted symmetry-forbidden connections with low transmission probabilities. Connection 5–8 of quinoline, connections 5–8 and 1–4 of isoquinoline, and connection 9–10 of benzo[g]quinoline and benzo[g]isoquinoline, which are indicated with thick arrows, are expected to be the best routs for electron transport. For connection 5–8 in quinoline, the product of the MO coefficients on atoms 5 and 8 in the HOMO is different from that in the LUMO and the orbital amplitudes of the HOMO and LUMO are relatively large. Therefore, the value of Eq. 11 is large and enhancement of the conductance occurs. For connections 3–6 and 2–7, the product of the MO coefficients on atoms 3 and 6 (2 and 7, respectively) in the HOMO has the same sign as in the LUMO. It is expected that those are symmetry-forbidden connections characterized by poor conductance. The same is true for benzo[g]quinoline, isoquinoline, and benzo[g]isoquinoline.

Figure 5 shows the transmission probabilities calculated by NEGF-HMO method for various connections of quinoline, isoquinoline, benzo[g]quinoline, and benzo[g]isoquinoline as a function of the electron energy. The solid lines show the symmetry-allowed connections, and the dashed lines show the symmetry-forbidden connections. Calculated transmission spectra show sharp peaks near the energy levels of the MO because the zeroth Green's function increases near those energies. The computational results are consistent with the qualitative predictions based on orbital symmetry discussion. The connections that are predicted to be symmetry-allowed for electron transport show high transmission probabilities at the Fermi energy. Connection 5–8 of quinoline, connections 5–8 and 1–4 of isoquinoline, connection 9–10 of benzo[g]quinoline, and connection 9–10 of benzo[g]isoquinoline are the best routes of the corresponding molecules with highest transmission probabilities. The predicted symmetry-forbidden connections show very low transmission probabilities. The shifts of the transmission spectra for symmetry-forbidden connection 2–7 in quinoline, 3–6 in isoquinoline, 2–7 in benzo[g]quinoline, and 3–6 in benzo[g]isoquinoline are due to the perturbations due to the N atoms. The explanation is similar to the one provided for connections 2–4 and 2–6 of pyridine. Overall, the NEGF-HMO results for those heterocyclic aromatic hydrocarbons confirm the orbital view predictions.

To confirm the heteroatomic effects derived with the orbital symmetry rule and NEGF–HMO level of theory, we applied the NEGF–DFT method implemented in the ATK 2008.10 program to more realistic models. Computed transmission spectra of pyridine dithiolates for different connection sites at zero bias as well as the corresponding *I–V* curves are shown in Fig. 6. In the transmission spectra, the Fermi energy is located at the origin of the energy $E = 0$, which was determined from DFT calculations of the bulk gold electrodes and the obtained transmission probabilities were aligned to it. For 2,5-pyridine dithiolate, expected as a symmetry-allowed connection, the transmission probability at the Fermi energy at zero bias is 0.892, whereas those for 2,4-, 2,6-, and 3,5-pyridine dithiolates at the Fermi energy at zero bias are small, with values of 0.039, 0.070, and 0.068, respectively. When the

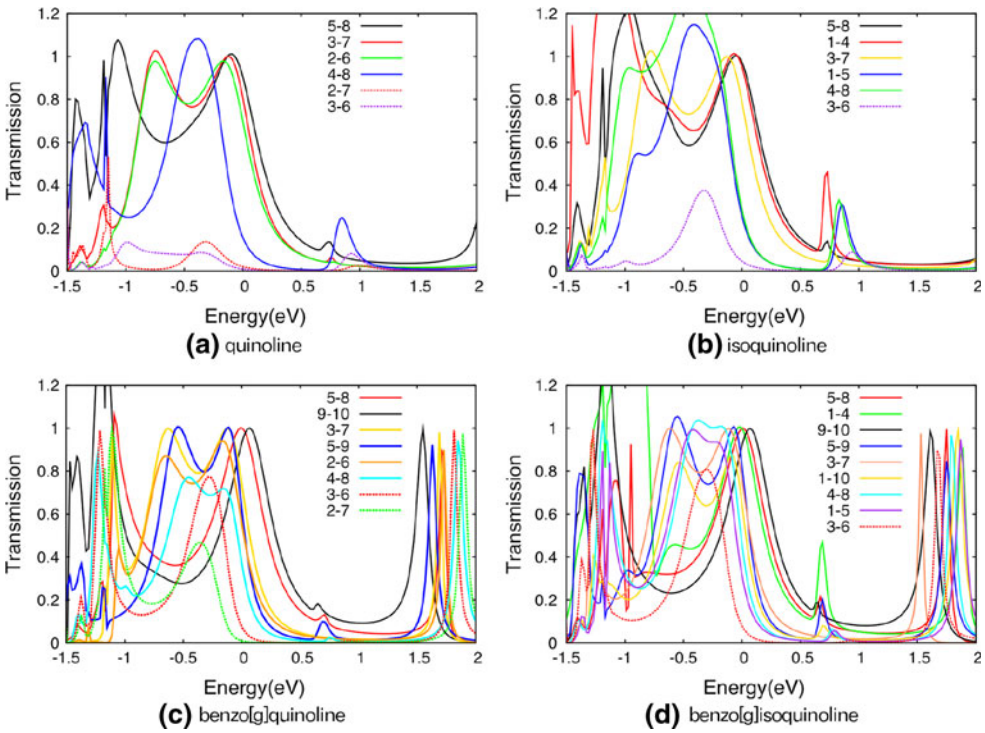

Fig. 7 Calculated transmission spectra at the zero bias for dithiolate junctions at the Perdew–Zunger LDA level of theory: **a** quinoline, **b** isoquinoline, **c** benzo[g]quinoline, and **d** benzo[g]isoquinoline

applied bias was is in the range from 0.0 to 1.0 V to the molecular junctions, the steady current was calculated by NEGF-DFT method with the following formula:

$$I(V) = \frac{2e}{h} \int_{\mu_R}^{\mu_L} [f(E-\mu_L) - f(E-\mu_R)]T(E,V)\mathrm{d}E, \qquad (15)$$

where $T(E,V)$ is the transmission probability as a function of energy E and the bias V, f is the Fermi function, and μ_L and μ_R are the electrochemical potentials of the left electrode and the right electrode, respectively. Only electrons with energy within a range near the Fermi energy can contribute to the total current. Therefore, the range of the bias window can be approximated by $[-V/2, +V/2]$ [20, 41]. Since the current is the integral of the transmission probabilities in the bias window, analysis of it may give us a clear understanding of the electron transport behavior. In view of I–V curves as shown in Fig. 6, only 2,5-pyridine dithiolate gave high values of the current with the applied bias, while the other dithiolates gave very low values. These DFT results are in good agreement with our qualitative predictions made from the orbital analysis based on orbital symmetry rule.

Further NEGF-DFT calculations were performed for the dithiolates of quinoline, isoquinoline, benzo[g]quinoline, and benzo[g]isoquinoline. The transmission spectra at the zero bias and I–V curves for these molecular junctions are shown in Figs. 7 and 8, respectively. The results show that the predicted symmetry-allowed connections for the corresponding dithiolates are indeed favorable for electron transport. These results are in good agreement with the qualitative orbital predictions. 5,8-Quinoline dithiolate has the highest conductance among the dithiolate derivatives of quinoline, and 5,8- and 1,4-isoquinoline dithiolates show the similar highest conductance among the isoquinoline dithiolate derivatives. For benzo[g]quinoline, dithiolate derivative 9–10 shows the best conductance; and 1,4-, 5,8-, and 9,10-benzo[g]isoquinoline dithiolates are the most favorable for electron transport in benzo[g]isoquinoline dithiolates. The symmetry-forbidden connections, 2–7 and 3–6 in quinoline and benzo[g]quinoline, 3–6 in isoquinoline and benzo[g]isoquinoline, for which we expected poor electron-transport properties, show low transmission probabilities and very poor conductance. Overall, the results of the computed transmission probabilities and I–V curves with NEGF-DFT method are in good agreement with those of the qualitative predictions with orbital symmetry rule.

4 Conclusions

We have applied the orbital symmetry rule to investigate the electron-transport properties of heterocyclic aromatic hydrocarbons. Connecting sites suitable for good electron-transport properties were predicted for pyridine, quinoline, isoquinoline, benzo[g]quinoline, and benzo[g]isoquinoline by looking at the phases and amplitudes of their frontier orbitals based on the orbital symmetry rule. In this way, we have expanded the applicability of the orbital symmetry rule to yet another type of molecules. After documenting it use for electron-transport properties of small aromatic

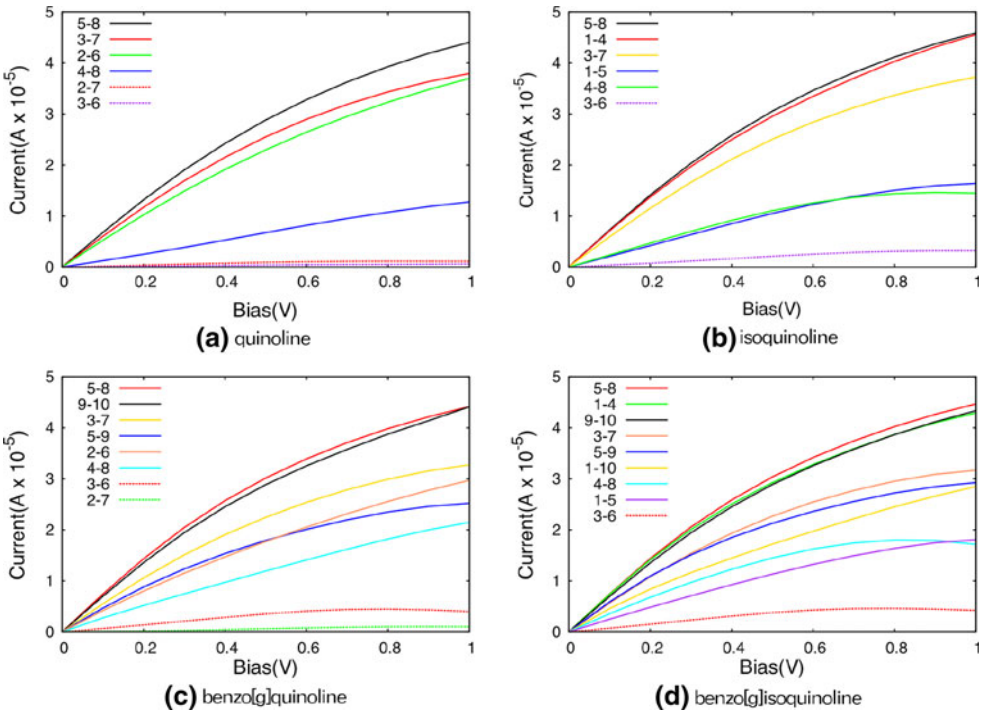

Fig. 8 Calculated *I–V* curves for dithiolate junctions at the Perdew–Zunger LDA level of theory: **a** quinoline, **b** isoquinoline, **c** benzo[g]quinoline, and **d** benzo[g]isoquinoline

hydrocarbons, larger PAHs with different edge types, and diarylethenes, all strongly coupled with the electrodes systems, we are now confident that the orbital symmetry rule can be used for the prediction of the electron-transport properties of other heterocyclic aromatic molecules. With this simple symmetry rule in mind, it is possible to approach large PAHs and nanographenes with heteroatomic defects, which are widely used in the fabrication of nanoscale transistors. This study demonstrates that the orbital symmetry rule is applicable to those systems and the observed deviations from it could be understood and explained. However, the introduction of heteroatoms in the aromatic compounds can induce perturbations to the energy spectra of the hydrocarbons and the transmission spectra of the junctions. The applied bias NEGF-DFT calculations and the computed *I–V* curves clearly demonstrate that the best routes for electron transport, predicted by simply looking at the frontier orbitals of the isolated hydrocarbons, are indeed the best conductance channels of the realistic metal–molecule–metal junctions. The effects of the heteroatomic perturbations diminish for larger hydrocarbons. The orbital symmetry rule is a very powerful tool to use for understanding and for rational design of molecular devices in experimental studies.

Acknowledgments K. Y. acknowledges Grants-in-Aid (Nos. 18GS0207 and 22245028) for Scientific Research from Japan Society for the Promotion of Science (JSPS) and the Ministry of Education, Culture, Sports, Science and Technology of Japan (MEXT), the Nanotechnology Support Project of MEXT, the MEXT Project of Integrated Research on Chemical Synthesis, and the Kyushu University Global COE Project for their support of this work. A. S. acknowledges JSPS for a postdoctoral fellowship.

References

1. Castro Neto AH, Guinea F, Peres NMR, Novoselov KS, Geim AK (2009) Rev Mod Phys 81:109–162
2. Wu JS, Pisula W, Müllen K (2007) Chem Rev 107:718–747
3. Dorogi M, Gomez J, Osifchin R, Andres RP, Reifenberger R (1995) Phys Rev B 52:9071–9077
4. Andres RP, Bein T, Dorogi M, Feng S, Henderson JI, Kubiak CP, Mahoney W, Osifchin RG, Reifenberger R (1996) Science 272:1323–1325
5. Xu BQ, Tao NJ (2003) Science 301:1221–1223
6. Xiao XY, Xu BQ, Tao NJ (2004) Nano Lett 4:267–271
7. Xu BQ, Xiao X, Tao NJ (2003) J Am Chem Soc 125:16164–16165
8. Huang ZF, Xu BQ, Chen YC, Di Ventra M, Tao NJ (2006) Nano Lett 6:1240–1244
9. Reed MA, Zhou C, Muller CJ, Burgin TP, Tour JM (1997) Science 278:252–254
10. Muller CJ, Vanruitenbeek JM, de Jongh LJ (1992) Physica C 191:485–504
11. Dulić D, van der Molen SJ, Kudernac T, Jonkman HT, de Jong JJD, Bowden TN, van Esch J, Feringa BL, van Wees BJ (2003) Phys Rev Lett 91:207402
12. Chen F, Tao NJ (2009) Acc Chem Res 42:429–438
13. Chen F, Hihath J, Huang ZF, Li XL, Tao NJ (2007) Annu Rev Phys Chem 58:535–564
14. Seideman T, Guo H (2003) J Theor Comp Chem 2:439–458
15. Xue Y, Ratner MA (2005) Int J Quantum Chem 102:911–924
16. Lindsay SM, Ratner MA (2007) Adv Mater 19:23–31
17. Petrov EG, Hänggi P (2001) Phys Rev Lett 86:2862–2865
18. Hettler MH, Schoeller H, Wenzel W (2002) Europhys Lett 57:571–577

19. Hsu LY, Jin BY (2009) Chem Phys 355:177–182
20. Brandbyge M, Mozos JL, Ordejon P, Taylor J, Stokbro K (2002) Phys Rev B 65:165401
21. Landauer R (1957) IBM J Res Dev 1:223–231
22. Staykov A, Nozaki D, Yoshizawa K (2007) J Phys Chem C 111:11699–11705
23. Staykov A, Nozaki D, Yoshizawa K (2007) J Phys Chem C 111:3517–3521
24. Andrews DQ, Van Duyne RP, Ratner MA (2008) Nano Lett 8:1120–1126
25. Quek SY, Kamenetska M, Steigerwald ML, Choi HJ, Louie SG, Hybertsen MS, Neaton JB, Venkataraman L (2009) Nature Nanotech 4:230–234
26. Quek SY, Choi HJ, Louie SG, Neaton JB (2009) Nano Lett 9:3949–3953
27. Yasuda S, Yoshida S, Sasaki J, Okutsu Y, Nakamura T, Taninaka A, Takeuchi O, Shigekawa H (2006) J Am Chem Soc 128:7746–7747
28. Ko C-H, Huang M-J, Fu M-D, Chen C-H (2009) J Am Chem Soc 132:756–764
29. Zhou JF, Chen GJ, Xu BQ (2010) J Phys Chem C 114:8587–8592
30. Cohen R, Stokbro K, Martin JML, Ratner MA (2007) J Phys Chem C 111:14893–14902
31. Solomon GC, Herrmann C, Hansen T, Mujica V, Ratner MA (2010) Nature Chemistry 2:223–228
32. Siddarth P, Marcus RA (1992) J Phys Chem 96:3213–3217
33. Markussen T, Stadler R, Thygesen KS (2010) Nano Lett 10:4260–4265
34. Tada T, Yoshizawa K (2002) ChemPhysChem 3:1035–1037
35. Tada T, Yoshizawa K (2003) J Phys Chem B 107:8789–8793
36. Tada T, Yoshizawa K (2004) J Phys Chem B 108:7565–7572
37. Yoshizawa K, Tada T, Staykov A (2008) J Am Chem Soc 130:9406–9413
38. Tsuji Y, Staykov A, Yoshizawa K (2009) J Phys Chem C 113:21477–21483
39. Tsuji Y, Staykov A, Yoshizawa K (2009) Thin Solid Films 518:444–447
40. Li XQ, Staykov A, Yoshizawa K (2010) J Phys Chem C 114:9997–10003
41. Datta S (1995) Electronic transport in mesoscopic systems. Cambridge University Press, Cambridge
42. Datta S (2005) Quantum transport: atom to transistor. Cambridge University Press, Cambridge
43. Caroli C, Combescot R, Nozieres P, Saint-James D (1971) J Phys C 4:916–929
44. Combescot R (1971) J Phys C 4:2611–2622
45. Tada T, Nozaki D, Kondo M, Hamayama S, Yoshizawa K (2004) J Am Chem Soc 126:14182–14189
46. Tsuji Y, Staykov A, Yoshizawa K (2011) J Am Chem Soc 133:5955–5965
47. Grönbeck H, Curioni A, Andreoni W (2000) J Am Chem Soc 122:3839–3842
48. Levine IN (2000) Quantum chemistry. Prentice-Hall International Inc., London
49. ATK, version 2008.10. QuantumWise. Conpenhagen, Denmark, http://www.quantumwise.com
50. Frisch MJ, Trucks GW, Schlegel HB, Scuseria GE, Robb MA, Cheeseman JR, Montgomery JA Jr, Vreven T, Kudin KN, Burant JC, Millam JM, Iyengar SS, Tomasi J, Barone V, Mennucci B, Cossi M, Scalmani G, Rega N, Petersson GA, Nakatsuji H, Hada M, Ehara M, Toyota K, Fukuda R, Hasegawa J, Ishida M, Nakajima T, Honda Y, Kitao O, Nakai H, Klene M, Li X, Knox JE, Hratchian HP, Cross JB, Bakken V, Adamo C, Jaramillo J, Gomperts R, Stratmann RE, Yazyev O, Austin AJ, Cammi R, Pomelli C, Ochterski JW, Ayala PY, Morokuma K, Voth GA, Salvador P, Dannenberg JJ, Zakrzewski VG, Dapprich S, Daniels AD, Strain MC, Farkas O, Malick DK, Rabuck AD, Raghavachari K, Foresman JB, Ortiz JV, Cui Q, Baboul AG, Clifford S, Cioslowski J, Stefanov BB, Liu G, Liashenko A, Piskorz P, Komaromi I, Martin RL, Fox DJ, Keith T, Al-Laham MA, Peng CY, Nanayakkara A, Challacombe M, Gill PMW, Johnson B, Chen W, Wong MW, Gonzalez C, Pople JA (2004) Gaussian 03, version E.01. Gaussian Inc., Wallingford CT
51. Becke AD (1993) J Chem Phys 98:5648–5652
52. Lee CT, Yang WT, Parr RG (1988) Phys Rev B 37:785–789
53. Vosko SH, Wilk L, Nusair M (1980) Can J Phys 58:1200–1211
54. Krishnan R, Binkley JS, Seeger R, Pople JA (1980) J Chem Phys 72:650–654
55. Hay PJ, Wadt WR (1985) J Chem Phys 82:270–283